ACS SENSORS

pubs.acs.org/acssensors Article

Characterization of Protein Aggregation Using Hydrogel-Encapsulated nIR Fluorescent Nanoparticle Sensors

Daniel P. Salem, Xun Gong, Heejin Lee, Alicia Zeng, Gang Xue, Jeff Schacherl, Scott Gibson, and Michael S. Strano*

Cite This: https://dx.doi.org/10.1021/acssensors.9b01586 Read Online

ACCESS | Metrics & More | Article Recommendations | Supporting Information

ABSTRACT: The monitoring of biopharmaceutical critical quality attributes in-process, at both the process development and manufacturing stages, is necessary for the implementation of process analytical technology and quality-by-design principles. Among these attributes, it is important to monitor and control protein aggregation during the manufacturing of biological therapeutics to prevent adverse immunogenic responses and minimize negative impacts on drug deliverability. In this work, we explore hydrogel-encapsulated, label-free fluorescent nanosensors for the characterization of protein aggregation. A mathematical model is used to describe the diffusion and binding of a series of stressed pharmaceutical samples to such sensors, describing their dynamic response. We use mathematical modeling to map the influence of hydrogel properties on the separation performance, given the composition of UV-stressed IgG_1 samples. Using this modified model, the compositions of light-stressed IgG_1 samples were fit to experimental data and correlated with size-exclusion chromatography data. The results demonstrate the ability to detect the presence of high-molecular-weight protein species at a concentration as low as 1%. This work represents a significant step toward the development and deployment of rapid process analytical technologies for biopharmaceutical characterization.

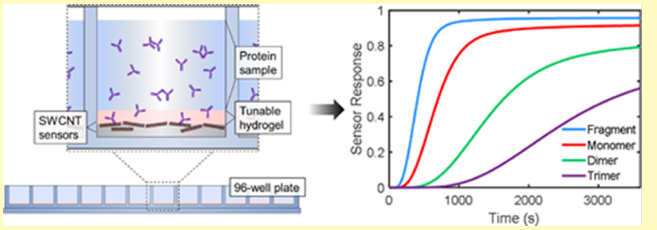

KEYWORDS: *single-walled carbon nanotube, SWCNT, biosensor, nanosensor, biopharmaceutical characterization, biopharmaceutical aggregation*

Downloaded via UNIV OF GOTHENBURG on January 30, 2020 at 09:34:28 (UTC).
See https://pubs.acs.org/sharingguidelines for options on how to legitimately share published articles.

The monitoring of biopharmaceutical critical quality attributes (CQAs) in-process, at both the process development and manufacturing stages, is necessary for the implementation of process analytical technology (PAT) and quality-by-design (QbD) principles.[1−4] Macromolecular therapeutics are much more challenging to characterize than traditional small-molecule drugs, as each analytical technique deployed provides a limited snapshot of the molecule's physical/chemical structure and function.[5] In addition, there remains limited first-principles understanding of the complex bioprocesses taking place during biopharmaceutical manufacturing, including how critical process parameters ultimately influence the properties of the final product.[1] Over the last 20 years, a great deal of research effort has focused on transitioning biopharmaceutical manufacturing processes from batch-based to continuous.[6−8] This shift has the potential to significantly reduce the footprint of manufacturing facilities while enabling a more modular process design that provides more flexibility for manufacturers. However, the realization of continuous manufacturing, in addition to the real-time release, requires rapid analytical technologies that can enable the implementation of process-control strategies and evaluate the quality of the produced drug on-line, in-line, or at-line.[1,9] Here, we report the development of a novel nanosensor platform consisting of hydrogel-encapsulated near-infrared (nIR)-fluorescent nanoparticles for the rapid (<20 min) characterization of protein aggregation. This tunable hydrogel influences the diffusion of the analyte to the sensors, allowing us to identify the presence of aggregate species through changes in the sensor response dynamics.

The aggregation state of protein therapeutics is a CQA that must be monitored and controlled throughout the manufacturing process as well as during storage.[10,11] Proteins exhibit limited stability in solution and can undergo aggregation in response to various stressors including temperature, light, shear, and changes in solution conditions (e.g., ionic strength, pH).[10,12−15] In addition to influencing the viscosity of the protein formulation,[16,17] protein aggregates may induce immunogenic responses upon administration in patients[18−20] and negatively impact drug deliverability.[21] As a result, the concentration of microscopically visible and subvisible particles must be carefully monitored, and protein formulations must be

Received: August 16, 2019
Accepted: January 9, 2020

© XXXX American Chemical Society

designed to limit the extent of protein aggregation when properly stored.

Proteins can undergo aggregation via a series of different reaction mechanisms, which ultimately determine the size and shape of the resulting particles.[11,16] The reaction mechanism that dominates within a particular system is influenced by the protein itself as well as the stressors at play.[11,12,15] In general, physical aggregation involves a series of reversible and irreversible steps that include the unfolding of protein regions and the formation of noncovalent protein bonds via the interaction of hydrophobic sections of amino acids.[12] The resulting size distribution is a product of competing reactions ranging from monomer−monomer nucleation to aggregate−aggregate coalescence, where aggregate particles can range from 10 nm to greater than 10 μm.[16]

Many analytical techniques are used to characterize protein aggregation[22] with differing levels of complexity and assay time including size-exclusion chromatography,[23,24] capillary electrophoresis,[25,26] and dynamic light scattering.[25,27,28] These techniques vary in the amount and resolution of structural and size information that they provide, with no single analytical technique being capable of fully elucidating the protein size distribution.[5,12,29] Nevertheless, there remains a need for new analytical technologies capable of rapid and/or continuous monitoring of protein aggregation for deployment within the biopharmaceutical manufacturing process in-line, on-line, or at-line. Such technologies would assist in the understanding and development of new bioprocesses, in addition to enabling feedback process-control techniques to be implemented at the manufacturing level.[1,9]

Single-walled carbon nanotube (SWCNT)-based optical sensors are a promising approach toward rapid, label-free biopharmaceutical characterization and have been developed for glycoprotein characterization,[30−32] biomarker detection,[33] and characterization of protein-binding interactions.[34] Their optical readout is well suited for sensor multiplexing, which was recently demonstrated by our group, in which nanosensor arrays were fabricated and characterized for protein detection.[35] Moreover, SWCNT nIR fluorescence does not photobleach over time, enabling the deployment of reversible sensors within continuous processes. Previously, our group reported the detection of human immunoglobulin G (IgG) using protein A-functionalized sensors embedded in a hydrogel matrix.[34] We found that protein A−IgG binding deviates from a simple monovalent kinetic model due to the multivalency of the binding interaction, resulting in an effective dissociation constant, $K_{D,eff}$, which varies with the protein concentration. Moreover, we formulated a bivalent binding model that could describe this phenomenon while comparing this result with the 1:1 binding observed between recombinant human growth hormone and its receptor.[34]

In this work, we report the development of an SWCNT-based sensor platform for the rapid detection of IgG_1 aggregation using protein A-functionalized sensors coupled with a tunable hydrogel matrix. Using a combination of modeling and experiment, we demonstrate the ability to control protein diffusion through the hydrogel matrix to the nanosensors and predict how protein diffusion is influenced by hydrogel properties. Experiments were performed using human IgG_1 that underwent UV light stress for varying lengths of time (3−74 h) and were characterized using size-exclusion ultra-high-performance liquid chromatography (SE-UPLC) and nanoparticle tracking analysis. We developed a mathematical model that is able to describe the experimental data generated from stressed IgG_1 samples, allowing us to extract compositional information from the sensor binding curves including the mole fraction of high-molecular-weight protein aggregates. Moreover, we find that the fitted compositions correlate with the data output by SE-UPLC, enabling the detection of high-molecular-weight species at concentrations as low as one percent on a molar basis. This work demonstrates that SWCNT-based optical sensors are a promising emerging technology for the rapid characterization of biopharmaceutical aggregation.

MATERIALS AND METHODS

Materials. All materials were purchased from Sigma-Aldrich unless stated otherwise. Highly purified CoMoCAT (6,5)-enriched SWCNTs were used for all experiments and were provided to us by Chasm Advanced Materials. Tissue culture-treated well plates were purchased from Genesee Scientific. Molecular biology agarose was purchased from Bio-Rad and recombinant Protein A (rPA, His-tagged at N-terminus) was purchased from Abcam. Human IgG_1 (conatumumab[36]) samples were provided to us by Amgen. IgG_1 samples were provided in a formulation buffer containing 10 mM sodium acetate and 9% sucrose, at a pH of 5.2.

Preparation and Characterization of SWCNT Dispersions. Approximately 1 mg of purified CoMoCAT SWCNTs was mixed with 15 mL of a 0.25 wt % chitosan solution in 1 vol % acetic acid. This solution was tip sonicated (Qsonica Q125) using a 0.25 in. probe for 40 min in an ice bath at 10 W. The crude SWCNT dispersion was centrifuged twice at 16 000g for 90 min, in which the top 80% of the supernatant was collected each time. The concentration of the purified SWCNT dispersion was approximated by collecting the absorption spectrum, which is provided in Supporting Information (Cary 5000, Agilent Technologies).

Sensor Fabrication and Functionalization. Sensors were fabricated using the same method as that outlined by Nelson et al.[34] Briefly, a 0.2% agarose solution was prepared in water and heated until the agarose had completely melted. Once the solution had cooled to about 50 °C, 50 μL aliquots were deposited on the bottom of a 96-well plate and allowed to cure in a humidified environment at room temperature for 45 min. Approximately 15 μL of 1 mg/L chitosan−SWCNT solution was added atop each gel and the well plate was placed in a humidified chamber at 38 °C for 45 min to promote the diffusion of SWCNTs into the hydrogel matrix. The well plate was later allowed to cool at room temperature for at least 10 min before washing each well with 150 μL of water to remove unbound SWCNTs.

Sensors were functionalized using a similar procedure as that reported previously.[30,33,34] First, a solution of 5 mg/mL succinic anhydride in 25× PBS was added atop the sensors to convert the primary amine groups into carboxylic acids. This reaction was allowed to proceed overnight. After washing the sensor gels two times with 150 μL of water, the carboxylic acid groups were activated by a solution of 20 mg/mL 1-ethyl-3-(3-dimethylaminopropyl)-carbodiimide (EDC) and 60 mg/mL *N*-hydroxysuccinimide (NHS) in MES buffer for 2 h. Following this activation step, the sensors were washed two times with 150 μL of water and reacted with a solution of approximately 14 mM Cu(II) chelated by N_α,N_α-bis(carboxymethyl)-L-lysine hydrate (Cu−NTA).

To create the Cu−NTA solution, 37 mg of N_α,N_α-bis-(carboxymethyl)-L-lysine hydrate (NTA) was combined with 170.5 mg of $CuCl_2{\cdot}2H_2O$ and 10 mL of 0.5× PBS. To precipitate out the excess, unchelated Cu(II) ions, the solution pH was increased to 7.5 via the addition of approximately 600 μL of 3 M NaOH. This solution was centrifuged at 1200 rpm for 7 min, after which the supernatant was used for reaction with the EDC/NHS-activated sensors.

Preparation of Stressed IgG_1 Samples. Stressed IgG_1 samples were prepared by exposing 100 mg/mL solutions of IgG_1 to UV light for varying periods of time including 3, 7, 26, 45, and 74 h. UV

https://dx.doi.org/10.1021/acssensors.9b01586
ACS Sens. XXXX, XXX, XXX−XXX

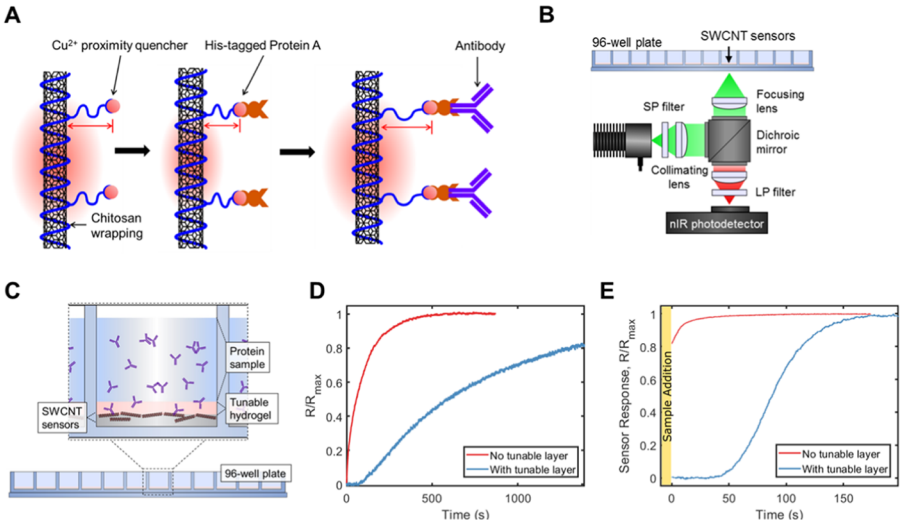

Figure 1. (A) Proposed schematic of the nIR fluorescent sensor mechanism. (B) Custom-built instrument used for performing inverted fluorescence excitation with a high-powered LED (880 mW) at 565 nm and collecting fluorescence from the underside of a standard 96-well plate into which the sensor and hydrogel are cast for each well;[34] LP and SP denote long pass and short pass, respectively. (C) Experimental design to detect protein aggregation where a tunable hydrogel layer influences the diffusion of the analyte to the sensors. Normalized nIR fluorescence sensor response, R/R_{max}, to (D) 10 mg/mL of human IgG_1 in PBS and (E) 10 mM EDTA in PBS with (blue) and without (red) an extra hydrogel layer of 0.2% agarose.

exposure was performed in a stability chamber equipped with a UVA lamp (wavelength range 320−400 nm) operating at a power of 22 W/m^2 at ambient temperature.

SWCNT Near-Infrared Fluorescence Measurements. SWCNT fluorescence measurements were collected using a single-channel nIR photodetector (ThorLabs, PDF10C).[34] Sensors were excited at 565 nm using a high-powered LED (ThorLabs, M565L3) and fluorescence was collected between 950 and 1050 nm using a 950 nm long-pass filter and a 1050 nm short-pass filter. Cu−NTA functionalized sensors were loaded with rPA at a concentration of 200 μg/mL in PBS for at least 15 min. After loading, the unbound protein was removed by washing the well with 150 μL of PBS. To remove artifacts associated with analyte mixing, IgG_1 solution was added directly atop the sensor hydrogels at a concentration of 10 mg/mL.

For experiments involving an extra tunable hydrogel layer above the sensors (Figure 1C), the hydrogel layer was added directly atop the washed sensor gel after rPA loading. The pore size and thickness of the tunable layer were controlled by modifying the agarose concentration and volume of agarose solution added atop the sensors, respectively. The agarose solution used for the tunable layer was kept at a constant temperature of 55 °C and was used the same day that it was prepared. Once the tunable hydrogel layer was added, it was allowed to cure at room temperature for at least 30 min before conducting an experiment. IgG_1-binding experiments involving a tunable hydrogel layer were conducted in the same way as outlined above, where an IgG_1 solution at a concentration of 10 mg/mL was added directly atop the hydrogel.

Nanoparticle Tracking Analysis. Nanoparticle tracking analysis was performed using a NanoSight Model LM10 manufactured by Malvern Instruments. IgG_1 samples were tested at a nominal concentration of 200 μg/mL and 20 videos were collected at 30 s per video. Analysis of the extracted particle trajectories was completed using a recently developed Bayesian model implemented in Matlab.[37]

RESULTS AND DISCUSSION

Sensor Development. An overview of the sensor detection mechanism is shown in Figure 1A and has been previously studied by our group.[34] Briefly, a series of functionalization reactions are performed to tether Cu−NTA groups to the chitosan wrapping, where the Cu(II) ion functions as a proximity quencher for SWCNT fluorescence.[34,38] The addition of hexahistidine-tagged recombinant protein A (rPA) causes a quenching response as the rPA binds to the Cu(II) ions, indicating that the entire complex moves closer to the SWCNT surface (Figure S2). This is consistent with previous work showing that protein A adsorbs to the surface of SWCNTs.[39] Upon IgG_1 binding to the Cu(II)/rPA complex, the sensors exhibit a turn-on fluorescence response as the Cu(II)−SWCNT distance increases.

SWCNT sensors were fabricated in a 96-well plate and measured using a custom-built nIR-fluorescence instrument shown in Figure 1B. Given that purified (6,5) SWCNTs were used for all experiments, sensors were excited at 565 nm using a high-powered LED to maximize the signal. Fluorescence was collected using a single-channel nIR photodetector.

Our approach to detect the presence of protein aggregates is shown in Figure 1C, in which a tunable hydrogel layer was added atop a sensor hydrogel layer to modulate the diffusion of the analyte. We hypothesized that as a greater fraction of a protein sample contained high-molecular-weight species, the transient sensor response may be delayed and exhibit different kinetics. To demonstrate this idea, we measured the sensor response to 10 mg/mL of human IgG_1 with and without a tunable layer containing 30 μL of 0.2% agarose. We define the sensor response, R, as the normalized change in SWCNT fluorescence, as defined by eq 1, where $I(t)$ is the fluorescence at time t and I_0 is the initial fluorescence intensity.

$$R(t) = \frac{I(t) - I_0}{I_0} \quad (1)$$

In addition, we define the normalized sensor response, R/R_{max}, as the sensor response, $R(t)$, divided by the maximum response, R_{max}. The results shown in Figure 1D demonstrate that the addition of a tunable layer causes a time lag in the sensor response as well as a slowing of the sensor response dynamics. To measure the effect of the tunable layer on small-molecule diffusion, we measured the sensor response to 10 mM EDTA. EDTA is known to cause a rapid turn-on response

https://dx.doi.org/10.1021/acssensors.9b01586
ACS Sens. XXXX, XXX, XXX−XXX

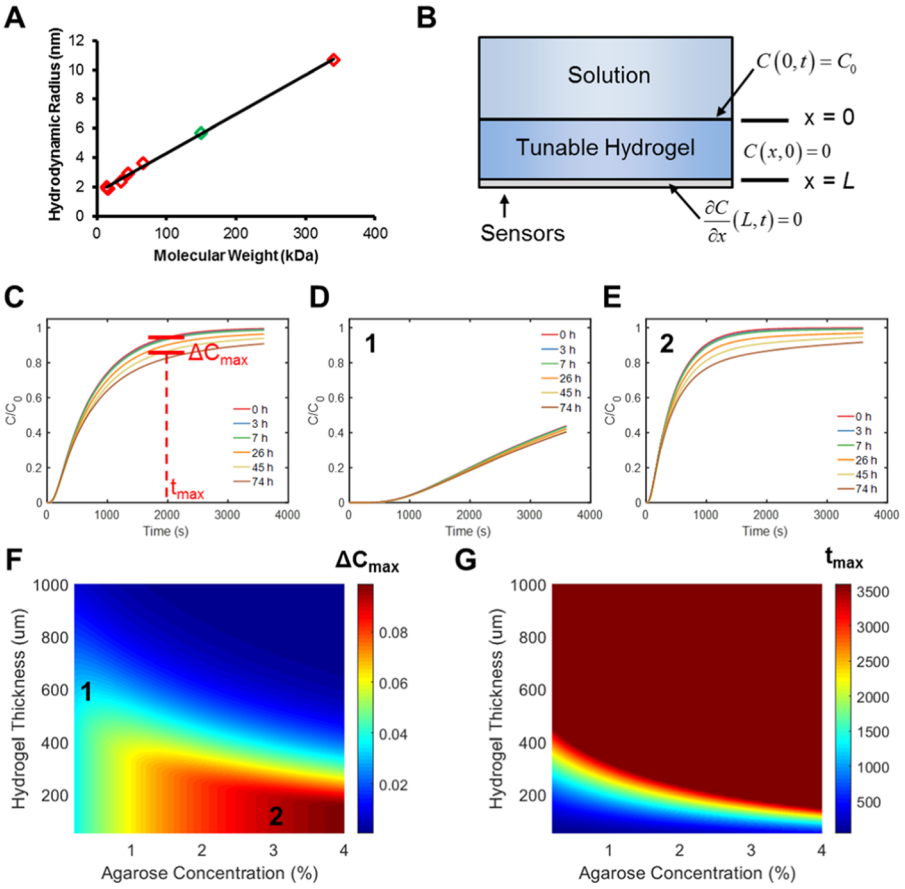

Figure 2. (A) Published hydrodynamic radii of nine different proteins (IgG shown in green) versus molecular weight[40,43] fitted to a linear correlation (R^2 = 0.993). (B) Schematic of the experimental system described by the diffusion model. (C) Graphical definition of ΔC_{max} and t_{max}. Concentration profiles at the agarose conditions of (D) 600 μm thickness, 0.2% concentration, and (E) 100 μm thickness, 3% concentration. (F) Simulated separation performance at various agarose concentrations and thicknesses of the extra tunable hydrogel layer. (G) Simulated time of maximum separation performance at various agarose concentrations and thicknesses.

as the EDTA outcompetes the NTA groups for the Cu(II) ions so that they are no longer tethered near the SWCNT surface. In the absence of a tunable layer, the addition of EDTA causes an immediate jump in the sensor signal that remains elevated over the course of several minutes (Figure 1E). However, as shown in Figure 1E, the addition of the tunable hydrogel layer causes a time lag in the sensor response and a slowing of the response dynamics such that the sensor response levels out only after several minutes. We note that the time scale of the experiment in Figure 1E is on the order of the diffusive time scale for a small molecule calculated via eq 2 below, assuming a hydrogel thickness of approximately 500 μm.

$$\tau_D = \frac{L^2}{D} \sim \frac{(500\ \mu\text{m})^2}{1 \times 10^{-5}\text{cm}^2/\text{s}} = 250\ \text{s} \tag{2}$$

Model-Aided Sensor Design. In an effort to guide the design of the tunable hydrogel layer, we developed a diffusion model to predict the diffusion of monomeric, low-molecular-weight (LMW) and high-molecular-weight (HMW) species to the sensors. For this analysis, we assumed that the protein solution was dilute and the diffusion of each species in the hydrogel was uncoupled. To estimate the diffusion coefficients, $D_{g,i}$, of all three species through the extra hydrogel layer, one of several different correlations can be used, all of which are influenced by the hydrogel pore size and protein hydrodynamic radius.[40] Given our choice of agarose as the hydrogel material, we used Amsden's model[40,41] to estimate the diffusion coefficients as described by eq 3 below, which is an obstruction-based model that has been demonstrated to work well when describing protein diffusion in agarose hydrogels.[42]

$$\frac{D_g}{D_0} = \exp\left[-\pi\left(\frac{r_s + r_f}{k_s\varphi^{-1/2} + 2r_f}\right)^2\right] \tag{3}$$

In eq 3, D_0 is the diffusion coefficient in solution (calculated using the Stokes–Einstein equation), r_s is the hydrodynamic radius of the solute, r_f is the radius of the polymer fiber (estimated at 19 Å),[40] φ is the volume fraction of agarose in the gel, and k_s is a hydrogel-specific scaling parameter (assumed to be 13.75 Å for agarose).[42] The volume fraction of agarose was calculated using eq 4,[42] where w is the weight fraction of agarose in the gel, ρ is the density of dry agarose (1.64 g/mL), and m is the mass fraction of agarose in an agarose hydrogel fiber (0.625).[42,43]

$$\varphi = \frac{w}{\rho \cdot m} \tag{4}$$

To estimate the hydrodynamic radii of various IgG_1 HMW or LMW species, we plotted the published hydrodynamic radii of nine different proteins (including IgG) spanning a wide range of molecular weights and fit a linear correlation (Figure 2A).[40,43] As an approximation during our preliminary

https://dx.doi.org/10.1021/acssensors.9b01586
ACS Sens. XXXX, XXX, XXX−XXX

modeling work, we assumed that HMW species were dimers and LMW species were 1/2 fragments. The resulting hydrodynamic radii were approximated as 5.6, 3.6, and 9.6 nm for monomer, LMW, and HMW species, respectively.

Based on the graphic, boundary, and initial conditions specified in Figure 2B, we formulated a one-dimensional diffusion model. The normalized concentration of species i at the sensors can be described by the following equation.[44]

$$\frac{C_i(L,t)}{C_{i,0}} = 1 - \frac{4}{\pi}\sum_{n=0}^{\infty}\frac{(-1)^n}{2n+1}\exp\left(-\frac{D_{g,i}(2n+1)^2\pi^2 t}{4L^2}\right) \quad (5)$$

To simulate the concentration profiles versus time of IgG_1 samples containing a varying distribution of monomeric, HMW, and LMW species, we used the compositional information collected from SE-UPLC for IgG_1 samples that underwent different levels of stress via UV light. UV light has been shown to induce both physical and chemical aggregation through the formation of chemical cross-links,[45−47] conformational changes in the protein structure,[45,48] and oxidation of methionine and other residues.[46,48,49] IgG_1 samples were stressed at a concentration of 100 mg/mL for 3−74 h and the measured mass fractions of monomeric (main peak), HMW, and LMW species are presented in Table 1. To supplement the SE-UPLC data and further elucidate the size distributions of the stressed IgG1 material, we performed a nanoparticle tracking analysis on the stressed samples, which can identify aggregate species between 30 nm and 1 μm (Supporting Information).

Table 1. SE-UPLC Data from UV Light-Stressed IgG_1 Samples Providing the Fraction of Unaffected Sample (monomer), High-Molecular-Weight Aggregates (HMW), and Low-Molecular-Weight Fragments

	mass fraction		
stress duration (h)	monomer	HMW	LMW
0	0.973	0.0037	0.0232
3	0.9535	0.0241	0.0225
7	0.9391	0.0389	0.022
26	0.8584	0.1214	0.0203
45	0.7764	0.2036	0.02
74	0.6483	0.3065	0.0452

Using the SE-UPLC data, we could simulate the total molar concentration profile of a given IgG_1 sample as the weighted sum of the profiles for individual protein species, as shown by eq 7.

$$\frac{C}{C_0}(L,t) = \alpha_M\left(\frac{C}{C_0}\right)_M + \alpha_{HMW}\left(\frac{C}{C_0}\right)_{HMW} + \alpha_{LMW}\left(\frac{C}{C_0}\right)_{LMW} \quad (6)$$

In eq 7, the three α_i parameters pertain to the mole fractions of monomer (M), HMW, and LMW species calculated from Table 1.

With the diffusion model fully developed, we defined two performance metrics of the tunable hydrogel layer: (A) the maximum concentration resolution and (B) the response time as defined below:

Criteria A

$$\Delta C_{max} = \max_t\left[\left(\frac{C}{C_0}\right)_{0h} - \left(\frac{C}{C_0}\right)_{45h}\right]$$

Criteria B

$$t_{max} = \text{time at which}(\Delta C = \Delta C_{max})$$

A graphical definition of these two parameters is shown in Figure 2C. Criteria A was chosen because the maximum concentration difference on the temporal curves directly correlates with the maximum potential sensor signal. Similarly, for practical reasons, users would prefer that the detection time be minimized for more real-time purposes. While the definition of ΔC_{max} is somewhat arbitrary regarding which two samples are being compared, we chose to use the 45-h stressed material as a reference, given that the concentration of LMW species in the 74-h stressed sample was anomalously high relative to the other samples (Table 1). In addition, using less stressed material as a reference sample would yield the same overall trends, albeit different values of ΔC_{max} and t_{max}.

In the case of choosing agarose as the hydrogel material, the two hydrogel properties that influence analyte diffusion are the concentration (i.e., pore size) and the thickness. As a result, we systematically varied these hydrogel properties, simulated concentration profiles over the course of 1 h, and generated maps of separation performance, as shown in Figure 2F,G. The results indicate that separation performance, on a concentration basis, is optimized when using tunable hydrogel layers of high agarose concentration and low thickness. Figure 2D,E shows the concentration profiles of the various stressed samples under the conditions represented by the numbers 1 and 2 in Figure 2F, respectively. Note that the results shown in Figure 2F,G are influenced by the fact that we simulated the concentrations for up to 1 h. Thus, the ΔC_{max} values plotted indicate the maximum separation over the course of an hour, not the maximum separation possible at a given set of agarose pore size and thickness.

While the preceding results indicate that a thin and concentrated agarose gel would achieve optimal separation performance in terms of the total concentration at the sensors, the dependence observed in Figure 2F does not necessarily correspond to maximum sensor discrimination. In the case of SWCNT nIR fluorescent sensors, analyte diffusion must be coupled with sensor binding at the hydrogel boundary. For this model, we assumed a monovalent binding reaction between all IgG_1 species and our sensors (θ). Moreover, we assumed that the sensors did not consume enough analyte to modify the analyte concentration profile and further aggregation did not take place in the hydrogel. This results in the binding reaction given below.

$$IgG + \theta \underset{k_r}{\overset{k_f}{\rightleftarrows}} IgG - \theta$$

The concentration of each bound IgG_1 species can be described by eq 8.

$$\frac{d[IgG-\theta]}{dt} = k_f[IgG](\theta_T - [IgG-\theta]) - k_r([IgG-\theta]) \quad (7)$$

https://dx.doi.org/10.1021/acssensors.9b01586
ACS Sens. XXXX, XXX, XXX−XXX

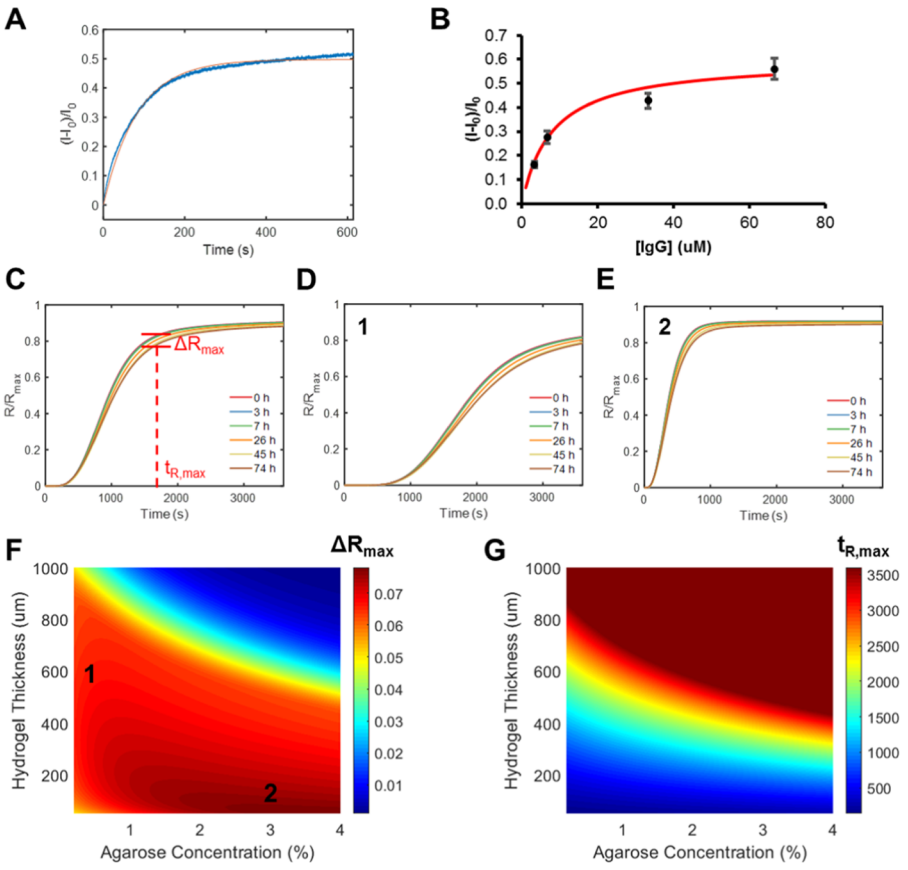

Figure 3. (A) Dynamic sensor binding data for 10 mg/mL unstressed IgG_1 collected without an extra hydrogel layer, along with a fit to a 1:1 sensor binding model. (B) Equilibrium sensor response data without an extra hydrogel layer at different IgG_1 concentrations, along with a fit to a 1:1 binding model. Error bars represent the standard deviations from three replicates. (C) Graphical definition of ΔR_{max} and $t_{R,max}$. Simulated sensor responses at the agarose conditions of (D) 600 μm thickness, 0.2% concentration, and (E) 100 μm thickness, 3% concentration. (F) Simulated sensor response separation performance at various agarose concentrations and thicknesses of the extra tunable hydrogel layer. (G) Simulated time of the maximum sensor response separation performance at various agarose concentrations and thicknesses.

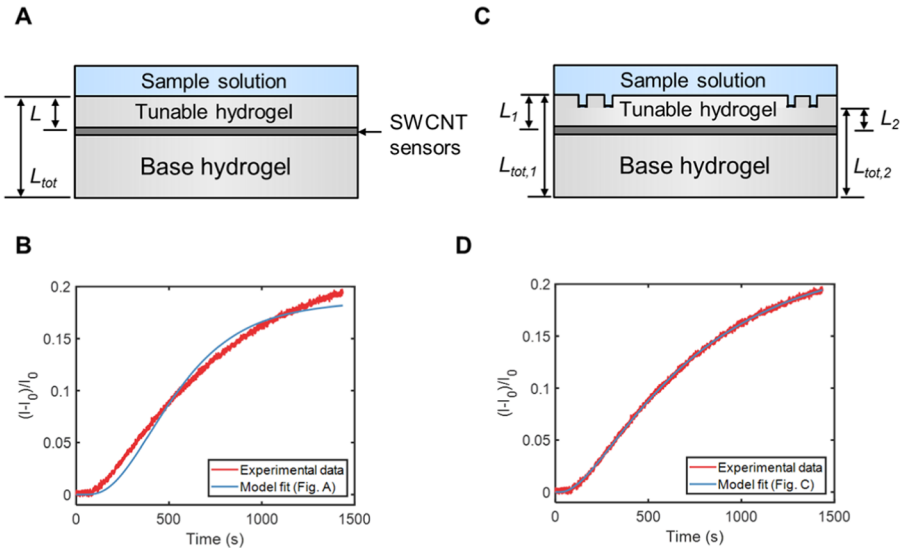

Figure 4. (A) Schematic of the experimental system where a single tunable hydrogel thickness is assumed. (B) Fit of the single-thickness model (eq 11) to experimental binding data collected for 10 mg/mL of unstressed human IgG_1 using a tunable layer of 30 μL of 0.2% agarose in a 96-well plate. (C) Schematic of the experimental system described by a two-thickness model that accounts for cracks that form within the hydrogel layer during casting and/or heterogeneity in the hydrogel thickness. (D) Fit of the two-thickness model (eqs 11 and 12) to the same experimental data shown in (B).

https://dx.doi.org/10.1021/acssensors.9b01586
ACS Sens. XXXX, XXX, XXX−XXX

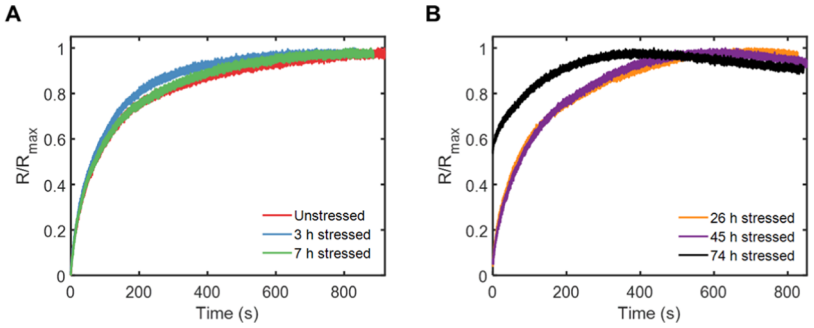

Figure 5. Normalized response of protein A-loaded sensors to 10 mg/mL of (A) unstressed IgG_1, 3-h stressed IgG_1, and 7-h stressed IgG_1, and (B) 26-h stressed IgG_1, 45-h stressed IgG_1, and 74-h stressed IgG_1. Experiments were performed without an extra tunable layer.

Normalizing each term in (8) by the total sensor concentration, θ_T, yields eq 9, which describes the fraction of bound sensor sites, f. This can ultimately be related to the sensor response, R, via eq 10, where R_{max} is equal to the maximum sensor response.

$$\frac{df}{dt} = k_f[\mathrm{IgG}](1-f) - k_r f \tag{8}$$

$$R = R_{max} \cdot f \tag{9}$$

To simulate the sensor response, eq 9 was coupled to the analyte diffusion model and solved numerically using the forward Euler method with a time step of one second. Based on data collected in the absence of a tunable layer using unstressed IgG_1, we used sensor parameter values of 0.6, 130 M^{-1} s^{-1}, and 8 μM for R_{max}, k_f, and K_D, respectively (Figure 3A,B).

With the combined diffusion and sensor binding model, we defined separation performance parameters based on the sensor output.

$$\text{A. } \Delta R_{max} = \max_t \left[\frac{R_{0h}}{R_{max}} - \frac{R_{45h}}{R_{max}} \right]$$

$$\text{B. } t_{R,max} = \text{time at which}(\Delta R = \Delta R_{max})$$

A graphical definition of these two parameters is shown in Figure 3C. Sensor responses were simulated assuming a bulk IgG_1 concentration of 10 mg/mL. Molar concentrations of IgG_1 were calculated using the average molecular weight approximated from the SE-UPLC data. Figure 3 shows the simulated sensor responses at the same conditions as Figure 2D,E, respectively. The maximum separation in sensor response is similar across many gel thicknesses and concentrations, with the main difference being the time at which the maximum separation is achieved (Figure 3G).

Application of the Model to Experimental Data. In addition to using the previously developed model to guide sensor design, we were ultimately interested in applying the model to experimental data to extract compositional information. Based on the results shown in Figure 3, we decided to use the same agarose concentration in the tunable layer as that used in the base layer (0.2%). A comparison of the sensor binding curves obtained from different agarose concentrations is provided in Supporting Information.

The schematic of the experimental system, shown in Figure 4A, can be described by the following solution to the diffusion equation, where L_{tot} is the total thickness of the tunable and base layers.[44] The thickness of the base layer was estimated by dividing the volume of the base layer by the cross-sectional area of the well bottom.

$$\frac{C(L,t)}{C_0} = 1 - \frac{4}{\pi}\sum_{n=0}^{\infty}\frac{(-1)^n}{2n+1}\exp\left(-\frac{D(2n+1)^2\pi^2 t}{4L_{tot}^{\ 2}}\right)\cos\left(\frac{(2n+1)\pi(L_{tot}-L)}{2L_{tot}}\right) \tag{10}$$

We coupled this equation to the sensor binding model discussed previously and fit experimental data collected from 10 mg/mL of unstressed IgG_1 using a tunable layer of 30 μL of 0.2% agarose. The composition of the IgG_1 sample was specified based on the SE-UPLC data and we fit the thickness of the tunable layer, L, and the maximum sensor response, R_{max}. The experimental data and resulting fit are shown in Figure 4B. While the coefficient of determination was calculated to be 0.986, systematic deviations between the experimental data and model fit can be observed. Specifically, we found that the as-formulated model predicts a larger time lag than was experimentally observed, in addition to faster response dynamics after the time lag. This result was consistent across all experiments.

To address the systematic deviations observed in Figure 4B, we developed a revised diffusion model that accounts for heterogeneity in the thickness of the tunable layer by approximating the system as having two effective thicknesses (Figure 4C). Heterogeneity in the tunable layer thickness could be caused by several factors including the formation of a meniscus with the well plate wall as well as the incomplete spreading of the agarose layer due to viscosity effects. The average concentration at the sensors could then be specified by an additional parameter, β, according to the following equation.

$$\frac{C}{C_0}(t) = (1-\beta)\cdot\left(\frac{C}{C_0}\right)_{L1} + \beta\cdot\left(\frac{C}{C_0}\right)_{L2} \tag{11}$$

In eq 12, $\left(\frac{C}{C_0}\right)_{L1}$ and $\left(\frac{C}{C_0}\right)_{L2}$ pertain to concentration profiles calculated from eq 11 using tunable layer thicknesses of L_1 and L_2, respectively (Figure 4C). As shown in Figure 4D, this revised model provides a significantly improved fit of the experimental data (coefficient of determination equal to 0.9995). A similar set of analyses was performed on the sensor response of a 2% agarose gel layer (Figure S5). Finally, 0.2% was chosen for ease of fabrication due to gel thickness.

Characterization of Gel Layers and Sensor Responses. The response of protein A-loaded SWCNT sensors

https://dx.doi.org/10.1021/acssensors.9b01586
ACS Sens. XXXX, XXX, XXX−XXX

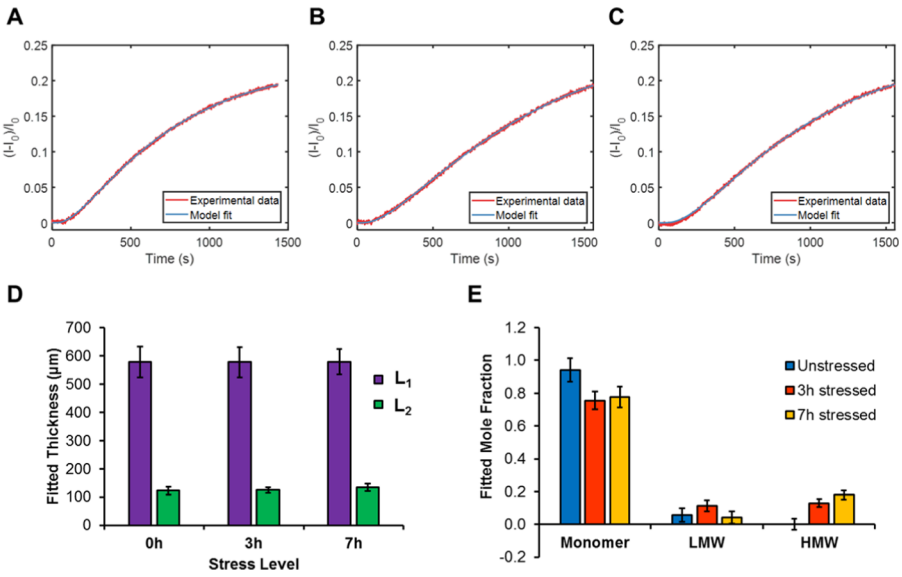

Figure 6. Sensors' response to 10 mg/mL of (A) unstressed IgG_1, (B) 3-h stressed IgG_1, and (C) 7-h stressed IgG_1 with a tunable hydrogel layer of 30 μL of 0.2% agarose. (D) Fitted L_1 and L_2 values for each dataset obtained by specifying the composition from the SE-UPLC data. Error bars represent the standard deviation from four replicates. (E) Fitted mole fractions of monomer, LMW, and HMW species using the L_1 and L_2 values fitted to the unstressed data. Error bars represent the 95% confidence intervals.

to the stressed IgG_1 samples was first evaluated in the absence of an extra tunable layer. All samples were tested at a nominal concentration of 10 mg/mL, and representative binding curves are shown in Figure 5 for all six samples. We observed that the sensors responded similarly to lower stressed IgG_1 samples (Figure 5A), suggesting that sensors without a tunable layer are unable to distinguish between low levels of stress. However, 26-, 45-, and 74-h stressed samples exhibited different response behaviors, with the sensor response decreasing at long time periods (Figure 5B). Furthermore, the addition of the 74-h stressed material caused an immediate, discontinuous sensor response, followed by a smaller binding curve (Figure 5B). While the reason for this response behavior is currently unknown, it is likely that the highly stressed samples contain a high concentration of oxidized species,[46,49] which have been shown to bind differently to protein A and protein G.[50] Moreover, the SE-UPLC results in Table 1 indicate that the concentration of LMW species is twice as high in the 74-h stressed sample versus the other samples, which may have also contributed to the anomalous sensor binding curve shown in Figure 5B.

The results shown in Figure 5B suggest that the more highly stressed IgG_1 samples contain a distribution of oxidized and/or higher-order aggregate species that are not accounted for in our initial mathematical model. Additionally, the HMW species in the UV-stressed samples are considered high as compared to biopharmaceuticals in production lines where the release specification for HMWs in protein therapeutics is normally $\leq$ 1%. As a result, we chose to limit our analysis to the low-stress protein material (unstressed, 3, and 7 h).

Figure 6A–C shows representative sensor responses to unstressed, 3-h stressed, and 7-h stressed IgG_1, respectively, using a tunable layer containing 30 μL of 0.2% agarose. IgG_1 samples were tested at a nominal concentration of 10 mg/mL, and exact concentrations were measured using UV absorption spectroscopy. Experimental data were fit to the previously developed two-thickness model by specifying the protein concentration and composition (from Table 1) and fitting the values of L_1, L_2, β, and R_{max}. The model fits are shown in Figure 6A–C along with the experimental data. The fitted L_1 and L_2 values were similar across all three samples, as shown in Figure 6D. Moreover, the L_1 values were of a similar magnitude to what would be expected based on the tunable layer volume and the microwell cross-sectional area. The fitted β and R_{max} values were also similar across the three samples and are provided in Supporting Information.

To extract compositional information from the experimental data, we fit the monomer, LMW, and HMW mole fractions using the L_1 and L_2 values fit from the unstressed data. The mole fractions were fit across an entire dataset (four replicates), while β and R_{max} were fit to each individual replicate. This was done so that the parameters β and R_{max} absorb any sensor-to-sensor variability that should not be attributed to the sample composition. The resulting fitted mole fractions are shown in Figure 6E. As expected, the fitted monomer mole fraction is much larger than the mole fractions of LMW and HMW species. Furthermore, the fitting procedure accurately predicts an increase in the concentration of HMW species with the stress level. The mole fraction of LMW species remains relatively constant across all three stress levels, which is consistent with the SE-UPLC data presented in Table 1. To evaluate the significance of these results, we performed one-way analysis of variance (ANOVA) across four independent datasets (four replicates per dataset), obtaining an F-ratio of 7.82 and a p value of 0.0107.

Extracting the mole fractions of three distinct diffusing species from a single binding curve (or a small set of binding curves) results in the relatively large confidence intervals shown in Figure 6E. While these confidence intervals, and the resulting assay resolution, can be improved by collecting more replicates or measuring sensor responses from multiple tunable layer designs, we investigated the implementation of a simplified, two-species model in which we assumed that the protein samples were composed of monomeric and HMW species. This simplified model may be more representative of our experimental system, given that the LMW species contain

https://dx.doi.org/10.1021/acssensors.9b01586
ACS Sens. XXXX, XXX, XXX−XXX

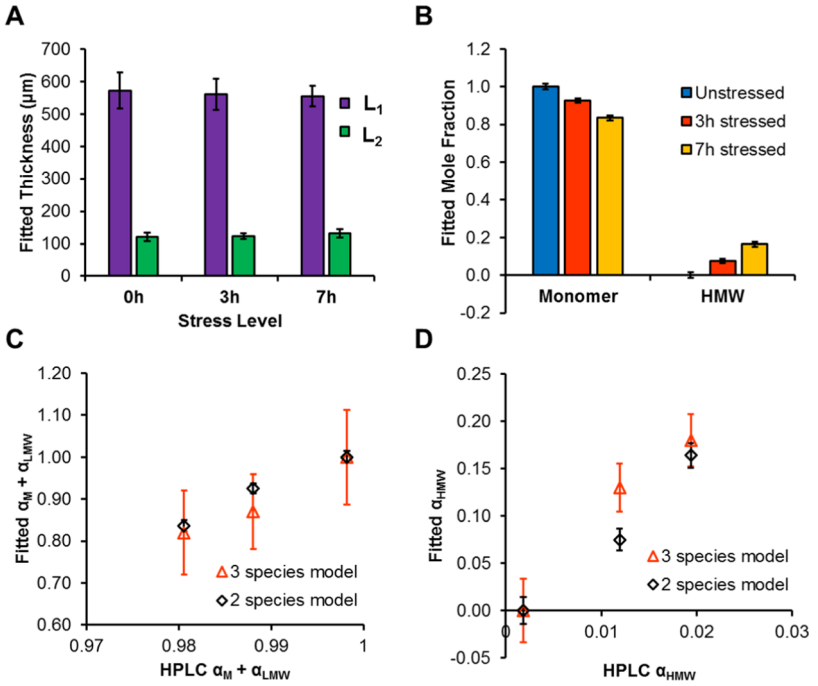

Figure 7. (A) Fitted L_1 and L_2 values for each dataset obtained by specifying the composition from SE-UPLC data, assuming a two-species system of monomer and HMW species. Error bars represent the standard deviation from four replicates. (B) Fitted mole fractions of monomer and HMW species using the L_1 and L_2 values fitted to the unstressed data. Error bars represent the 95% confidence intervals. Parity plot of (C) Monomer and LMW species, and (D) HMW species based on the SE-UPLC data and fitted values from the 3- and 2-species models. Error bars represent the 95% confidence intervals.

IgG_1 light chain and cleavage products that do not bind as strongly to protein A. Similarly to Figure 6D, we fit the L_1 and L_2 values for each stressed sample based on the compositional information provided by the SE-UPLC data. For this analysis, the monomer mole fraction was assumed to be the sum of the monomer and LMW mole fractions calculated from Table 1. The resulting fitted thicknesses are shown in Figure 7A and are very similar to those shown in Figure 6D. Moreover, the coefficients of determination were nearly identical to those obtained from the three-species model (>0.999), indicating that the goodness of fit was not reduced by the model simplification.

Using the fitted L_1 and L_2 values from the unstressed IgG_1 material, we fit the mole fractions of monomer and HMW species to all three datasets. As shown in Figure 7B, the simplified two-species model yields similar results as the three-species model shown in Figure 6D, with the model accurately fitting an increase in the HMW species concentration (and the corresponding decrease in the monomer concentration) with the stress level. Moreover, the 95% confidence intervals of the resulting fits are much smaller than those shown in Figure 6E. A one-way ANOVA analysis across four independent datasets yielded an F-ratio of 9.2 and a p value of 0.0067, confirming that our sensor system can distinguish between the low-stressed samples.

To compare both models with the SE-UPLC data, we constructed parity plots for the fitted mole fractions. Figure 7C compares the sum of the monomer and LMW mole fractions, while Figure 7D compares the HMW mole fractions. In both cases, the models are well correlated with the SE-UPLC data. While an exact 1:1 correlation is not obtained, such a correlation would be highly unlikely, given the assumptions of our model and the incomplete particle size distribution information obtained from SE-UPLC. Nevertheless, these results demonstrate the ability of our SWCNT sensor platform to detect levels of protein aggregation as low as one percent.

We note that the current formulation of the mathematical model describing our experimental setup assumes a very simple particle size distribution of monomers, dimers, and 1/2 fragments. While our 2- and 3-species models are able to well describe the experimental data, the stressed samples contain a wide distribution of particle shapes and sizes that span a range of diffusion coefficients within the tunable layer. Assuming species diffuse independently, greater elucidation of the particle size distribution is possible by simply incorporating more diffusing species into the mathematical model. However, as demonstrated in Figure 7C,D, extraction of compositional information with narrow confidence intervals would most likely require sensor multiplexing with more than one distinct tunable layer design. Given that sensor multiplexing can be performed in parallel, greater elucidation of the particle size distribution is possible without an increase in the assay time.

CONCLUSIONS

We report the development of a rapid analytical platform for the detection of protein aggregation using hydrogel-encapsulated, nIR-fluorescent SWCNT sensors. We demonstrate the feasibility of this approach by developing a diffusion model describing the transport of protein species to the sensor. By coupling the diffusion model to a sensor binding model, we are able to predict the sensor response at a given set of hydrogel properties and protein particle size distributions. Moreover, we use mathematical modeling to map the influence of hydrogel properties on the separation performance, given the composition of UV-stressed IgG_1 samples.

https://dx.doi.org/10.1021/acssensors.9b01586
ACS Sens. XXXX, XXX, XXX−XXX

Upon applying the mathematical model to experimental data collected from the stressed IgG_1 samples, we demonstrate that the data are well fit by a modified two-thickness model that accounts for heterogeneity in the thickness of the tunable hydrogel layer. Using this modified model, the compositions of UV-stressed IgG_1 samples were fit to experimental data and correlated with SE-UPLC data. The results demonstrate the ability to detect the presence of high-molecular-weight protein species at a concentration as low as 1%.

While this work represents a significant step toward the development and deployment of rapid process analytical technologies for biopharmaceutical characterization, several challenges guide our ongoing work. The current model and sensor assay do not account for the relative sizes of aggregates at this stage. We assume that all components of aggregates contribute equal responses. As a sensor design scheme, there may exist some fundamental limitations based on how much diffusion can be influenced and the sensor SNR, which would affect the maximum resolution of the size distribution we could discern. Also, we have yet to demonstrate the technique being used more rapidly. Finally, further development of the current sensor binding scheme involves testing against chemical modifications (i.e., oxidation) of IgG as well as an extension to other biopharmaceuticals. Lastly, while the current sensor form factor is sufficient as an assay on the factory floor, optical probe setups can potentially be designed to make such sensor schemes a part of the in-line process.

■ ASSOCIATED CONTENT

Supporting Information

The Supporting Information is available free of charge at https://pubs.acs.org/doi/10.1021/acssensors.9b01586.

AS_Supplement.docx – diffusion model derivation, particle size tracking analysis, additional nanosensor optical characterization, tunable layer composition, and response comparison (PDF)

■ AUTHOR INFORMATION

Corresponding Author

Michael S. Strano – *Department of Chemical Engineering, Massachusetts Institute of Technology, Cambridge, Massachusetts 02139, United States;* orcid.org/0000-0003-2944-808X; Email: strano@mit.edu

Authors

Daniel P. Salem – *Department of Chemical Engineering, Massachusetts Institute of Technology, Cambridge, Massachusetts 02139, United States*

Xun Gong – *Department of Chemical Engineering, Massachusetts Institute of Technology, Cambridge, Massachusetts 02139, United States;* orcid.org/0000-0003-4168-2768

Heejin Lee – *Process Development, Amgen Inc., Cambridge, Massachusetts 02142, United States*

Alicia Zeng – *Process Development, Amgen Inc., Cambridge, Massachusetts 02142, United States*

Gang Xue – *Process Development, Amgen Inc., Cambridge, Massachusetts 02142, United States*

Jeff Schacherl – *Process Development, Amgen Inc., Cambridge, Massachusetts 02142, United States*

Scott Gibson – *Process Development, Amgen Inc., Cambridge, Massachusetts 02142, United States*

Complete contact information is available at: https://pubs.acs.org/10.1021/acssensors.9b01586

Notes

The authors declare no competing financial interest.

■ ACKNOWLEDGMENTS

The authors are grateful for a grant from Amgen Inc. D.P. Salem is grateful for a National Science Foundation Graduate Research Fellowship. We also acknowledge Patrick Gammell, Jette Wypych, Linda Narhi, Tohid Pirbodaghi, Sheldon Moberg, Rohini Deshpande, and Bill Rich at Amgen for their constructive comments, guidance, and support.

■ ABBREVIATIONS

SWCNT, single-walled carbon nanotubes; nIR, near-infrared

■ REFERENCES

(1) Ündey, C.; Ertunc, S.; Mistretta, T.; Looze, B. Applied advanced process analytics in biopharmaceutical manufacturing: Challenges and prospects in real-time monitoring and control. *J. Process Control* **2010**, *20*, 1009–1018.

(2) Guidance for Industry: PAT—a Framework for Innovative Pharmaceutical Development, Manufacturing and Quality Assurance, (Food and Drug Administration, 2004).

(3) Glassey, J.; Gernaey, K. V.; Clemens, C.; Schulz, T. W.; Oliveira, R.; Striedner, G.; Mandenius, C. F. Process analytical technology (PAT) for biopharmaceuticals. *Biotechnol. J.* **2011**, *6*, 369–377.

(4) Rathore, A. S.; Bhambure, R.; Ghare, V. Process analytical technology (PAT) for biopharmaceutical products. *Anal. Bioanal. Chem.* **2010**, *398*, 137–154.

(5) Berkowitz, S. A.; Engen, J. R.; Mazzeo, J. R.; Jones, G. B. Analytical tools for characterizing biopharmaceuticals and the implications for biosimilars. *Nat. Rev. Drug Discovery* **2012**, *11*, 527–540.

(6) Croughan, M. S.; Konstantinov, K. B.; Cooney, C. The Future of Industrial Bioprocessing: Batch or Continuous? *Biotechnol. Bioeng.* **2015**, *112*, 648–651.

(7) Warikoo, V.; Godawat, R.; Brower, K.; Jain, S.; Cummings, D.; Simons, E.; Johnson, T.; Walther, J.; Yu, M.; Wright, B.; McLarty, J.; Karey, K. P.; Hwang, C.; Zhou, W. C.; Riske, F.; Konstantinov, K. Integrated continuous production of recombinant therapeutic proteins. *Biotechnol. Bioeng.* **2012**, *109*, 3018–3029.

(8) Crowell, L. E.; Lu, A. E.; Love, K. R.; Stockdale, A.; Timmick, S. M.; Wu, D.; Wang, Y.; Doherty, W.; Bonnyman, A.; Vecchiarello, N.; Goodwine, C.; Bradbury, L.; Brady, J. R.; Clark, J. J.; Colant, N. A.; Cvetkovic, A.; Dalvie, N. C.; Liu, D. N.; Liu, Y. J.; Mascarenhas, C. A.; Matthews, C. B.; Mozdzierz, N. J.; Shah, K. A.; Wu, S. L.; Hancock, W. S.; Braatz, R. D.; Cramer, S. M.; Love, J. C. On-demand manufacturing of clinical-quality biopharmaceuticals. *Nat. Biotechnol.* **2018**, *36*, 988.

(9) Hong, M. S.; Severson, K. A.; Jiang, M.; Lu, A. E.; Love, J. C.; Braatz, R. D. Challenges and opportunities in biopharmaceutical manufacturing control. *Comput. Chem. Eng.* **2018**, *110*, 106–114.

(10) Joubert, M. K.; Luo, Q. Z.; Nashed-Samuel, Y.; Wypych, J.; Narhi, L. O. Classification and Characterization of Therapeutic Antibody Aggregates. *J. Biol. Chem.* **2011**, *286*, 25118–25133.

(11) Roberts, C. J. Therapeutic protein aggregation: mechanisms, design, and control. *Trends Biotechnol.* **2014**, *32*, 372–380.

(12) Wang, W. Protein aggregation and its inhibition in biopharmaceutics. *Int. J. Pharm.* **2005**, *289*, 1–30.

(13) Luo, Q. Z.; Joubert, M. K.; Stevenson, R.; Ketchem, R. R.; Narhi, L. O.; Wypych, J. Chemical Modifications in Therapeutic Protein Aggregates Generated under Different Stress Conditions. *J. Biol. Chem.* **2011**, *286*, 25134–25144.

(14) Mahler, H. C.; Friess, W.; Grauschopf, U.; Kiese, S. Protein Aggregation: Pathways, Induction Factors and Analysis. *J. Pharm. Sci.* **2009**, *98*, 2909−2934.
(15) Hawe, A.; Kasper, J. C.; Friess, W.; Jiskoot, W. Structural properties of monoclonal antibody aggregates induced by freeze-thawing and thermal stress. *Eur. J. Pharm. Sci.* **2009**, *38*, 79−87.
(16) Amin, S.; Barnett, G. V.; Pathak, J. A.; Roberts, C. J.; Sarangapani, P. S. Protein aggregation, particle formation, characterization & rheology. *Curr. Opin. Colloid Interface Sci.* **2014**, *19*, 438−449.
(17) Pathak, J. A.; Sologuren, R. R.; Narwal, R. Do Clustering Monoclonal Antibody Solutions Really Have a Concentration Dependence of Viscosity? *Biophys. J.* **2013**, *104*, 913−923.
(18) Rosenberg, A. S. Effects of protein aggregates: An immunologic perspective. *Aaps J.* **2006**, *8*, E501−E507.
(19) Demeule, B.; Gumy, R.; Arvinte, T. Where disease pathogenesis meets protein formulation: Renal deposition of immunoglobulin aggregates. *Eur. J. Pharm. Biopharm.* **2006**, *62*, 121−130.
(20) Ripple, D. C.; Dimitrova, M. N. Protein particles: What we know and what we do not know. *J. Pharm. Sci.* **2012**, *101*, 3568−3579.
(21) Roberts, C. J. Protein Aggregation and Its Impact on Product Quality. *Curr. Opin. Biotechnol.* **2014**, *30*, 211−217.
(22) den Engelsman, J.; Garidel, P.; Smulders, R.; Koll, H.; Smith, B.; Bassarab, S.; Seidl, A.; Hainzl, O.; Jiskoot, W. Strategies for the Assessment of Protein Aggregates in Pharmaceutical Biotech Product Development. *Pharm. Res.* **2011**, *28*, 920−933.
(23) Hong, P.; Koza, S.; Bouvier, E. S. P. A Review Size-Exclusion Chromatography for the Analysis of Protein Biotherapeutics and Their Aggregates. *J. Liq. Chromatogr. Relat. Technol.* **2012**, *35*, 2923−2950.
(24) Fekete, S.; Beck, A.; Veuthey, J. L.; Guillarme, D. Theory and practice of size exclusion chromatography for the analysis of protein aggregates. *J. Pharm. Biomed. Anal.* **2014**, *101*, 161−173.
(25) Bermudez, O.; Forciniti, D. Aggregation and denaturation of antibodies: a capillary electrophoresis, dynamic light scattering, and aqueous two-phase partitioning study. *J. Chromatogr. B* **2004**, *807*, 17−24.
(26) Righetti, P. G.; Verzola, B. Folding/unfolding/refolding of proteins: Present methodologies in comparison with capillary zone electrophoresis. *Electrophoresis* **2001**, *22*, 2359−2374.
(27) Rosenqvist, E.; Jossang, T.; Feder, J. Thermal-Properties of Human-Igg. *Mol. Immunol.* **1987**, *24*, 495−501.
(28) Jossang, T.; Feder, J.; Rosenqvist, E. Heat Aggregation Kinetics of Human-Igg. *J. Chem. Phys.* **1985**, *82*, 574−589.
(29) Zölls, S.; Tantipolphan, R.; Wiggenhorn, M.; Winter, G.; Jiskoot, W.; Friess, W.; Hawe, A. Particles in therapeutic protein formulations, Part 1: Overview of analytical methods. *J. Pharm. Sci.* **2012**, *101*, 914−935.
(30) Reuel, N. F.; Ahn, J. H.; Kim, J. H.; Zhang, J. Q.; Boghossian, A. A.; Mahal, L. K.; Strano, M. S. Transduction of Glycan-Lectin Binding Using Near-Infrared Fluorescent Single-Walled Carbon Nanotubes for Glycan Profiling. *J. Am. Chem. Soc.* **2011**, *133*, 17923−17933.
(31) Reuel, N. F.; Grassbaugh, B.; Kruss, S.; Mundy, J. Z.; Opel, C.; Ogunniyi, A. O.; Egodage, K.; Wahl, R.; Helk, B.; Zhang, J. Q.; Kalcioglu, Z. I.; Tvrdy, K.; Bellisario, D. O.; Mu, B.; Blake, S. S.; Van Vliet, K. J.; Love, J. C.; Wittrup, K. D.; Strano, M. S. Emergent Properties of Nanosensor Arrays: Applications for Monitoring IgG Affinity Distributions, Weakly Affined Hypermannosylation, and Colony Selection for Biomanufacturing. *ACS Nano* **2013**, *7*, 7472−7482.
(32) Salem, D. P.; Nelson, J. T.; Kim, S.; Strano, M. S. A Dynamic, Mathematical Model for Quantitative Glycoprofiling Using Label-Free Lectin Microarrays. *ACS Sensors* **2016**, *1*, 987−996.
(33) Zhang, J. Q.; Kruss, S.; Hilmer, A. J.; Shimizu, S.; Schmois, Z.; De La Cruz, F.; Barone, P. W.; Reuel, N. F.; Heller, D. A.; Strano, M. S. A Rapid, Direct, Quantitative, and Label-Free Detector of Cardiac Biomarker Troponin T Using Near-Infrared Fluorescent Single-Walled Carbon Nanotube Sensors. *Adv. Healthcare Mater.* **2014**, *3*, 412−423.
(34) Nelson, J. T.; Kim, S.; Reuel, N. F.; Salem, D. P.; Bisker, G.; Landry, M. P.; Kruss, S.; Barone, P. W.; Kwak, S.; Strano, M. S. Mechanism of Immobilized Protein A Binding to Immunoglobulin G on Nanosensor Array Surfaces. *Anal. Chem.* **2015**, *87*, 8186−8193.
(35) Dong, J. Y.; Salem, D. P.; Sun, J. H.; Strano, M. S. Analysis of Multiplexed Nanosensor Arrays Based on Near-Infrared Fluorescent Single-Walled Carbon Nanotubes. *ACS Nano* **2018**, *12*, 3769−3779.
(36) LoRusso, P.; Hong, D.; Heath, E.; Kurzrock, R.; Wang, D.; Hsu, M.; Goyal, L.; Wiezorek, J.; Storgard, C.; Herbst, R. First-in-human study of AMG 655, a pro-apoptotic TRAIL receptor-2 agonist, in adult patients with advanced solid tumors. *J. Clin. Oncol.* **2007**, *25*, 3534.
(37) Silmore, K. S.; Gong, X.; Strano, M. S.; Swan, J. W. High Resolution Nanoparticle Sizing with Maximum A posteriori Nanoparticle Tracking Analysis (MANTA). *ACS Nano* **2018**, *13*, 3940.
(38) Brege, J. J.; Gallaway, C.; Barron, A. R. Fluorescence Quenching of Single-Walled Carbon Nanotubes with Transition-Metal Ions. *J. Phys. Chem. C* **2009**, *113*, 4270−4276.
(39) Chen, R. J.; Bangsaruntip, S.; Drouvalakis, K. A.; Kam, N. W. S.; Shim, M.; Li, Y. M.; Kim, W.; Utz, P. J.; Dai, H. J. Noncovalent functionalization of carbon nanotubes for highly specific electronic biosensors. *Proc. Natl. Acad. Sci. USA* **2003**, *100*, 4984−4989.
(40) Amsden, B. Solute diffusion within hydrogels. Mechanisms and models. *Macromolecules* **1998**, *31*, 8382−8395.
(41) Amsden, B. An obstruction-scaling model for diffusion in homogeneous hydrogels. *Macromolecules* **1999**, *32*, 874−879.
(42) Liang, S. M.; Xu, J.; Weng, L. H.; Dai, H. J.; Zhang, X. L.; Zhang, L. N. Protein diffusion in agarose hydrogel in situ measured by improved refractive index method. *J. Controlled Release* **2006**, *115*, 189−196.
(43) Pluen, A.; Netti, P. A.; Jain, R. K.; Berk, D. A. Diffusion of macromolecules in agarose gels: Comparison of linear and globular configurations. *Biophys. J.* **1999**, *77*, 542−552.
(44) Crank, J. *The Mathematics of Diffusion*, 2nd ed.; Oxford University Press, 1975.
(45) Mason, B. D.; Schöneich, C.; Kerwin, B. A. Effect of pH and Light on Aggregation and Conformation of an IgG1 mAb. *Mol. Pharmaceutics* **2012**, *9*, 774−790.
(46) Shah, D. D.; Zhang, J. M.; Maity, H.; Mallela, K. M. G. Effect of photo-degradation on the structure, stability, aggregation, and function of an IgG1 monoclonal antibody. *Int. J. Pharm.* **2018**, *547*, 438−449.
(47) Cockrell, G. M.; Wolfe, M. S.; Wolfe, J. L.; Schoneich, C. Photoinduced aggregation of a model antibody-drug conjugate. *Mol. Pharmaceutics* **2015**, *12*, 1784−1797.
(48) Liu, D.; Ren, D.; Huang, H.; Dankberg, J.; Rosenfeld, R.; Cocco, M. J.; Li, I.; Brems, D. N.; Remmele, R. L., Jr. Structure and stability changes of human IgG1 Fc as a consequence of methionine oxidation. *Biochemistry* **2008**, *47*, 5088−5100.
(49) Lorenz, C. M.; Wolk, B. M.; Quan, C. P.; Alcala, E. W.; Eng, M.; McDonald, D. J.; Matthews, T. C. The Effect of Low Intensity Ultraviolet-C Light on Monoclonal Antibodies. *Biotechnol. Prog.* **2009**, *25*, 476−482.
(50) Gaza-Bulseco, G.; Faidu, S.; Hurkmans, K.; Chumsae, C.; Liu, H. C. Effect of methionine oxidation of a recombinant monoclonal antibody on the binding affinity to protein A and protein G. *J. Chromatogr. B* **2008**, *870*, 55−62.

https://dx.doi.org/10.1021/acssensors.9b01586
ACS Sens. XXXX, XXX, XXX−XXX